Use of thresholding algorithms in the processing of raindrop imagery

D. D. Saxena and J. R. Saylor

Several thresholding algorithms are applied to the analysis of drop images, and their performance is compared. Images were obtained by use of a digital camera setup in which drops were illuminated from behind, resulting in an image of the drop silhouette. Each algorithm was evaluated based on the accuracy of the drop diameter obtained from the thresholded image and on the size of the depth of field. Because of the difficulty associated with creating drops that have a known diameter, solid spheres composed of a glass with an index of refraction close to that of water were used in computing the depth of field and in determining the accuracy of measured diameter. The application of this study is to the automatic measurement of raindrops and images were obtained during several storms. With each thresholding algorithm this raindrop imagery was used to compute the probability density function of drop diameter, and the rain rate. The performance of each thresholding algorithm was quantified by comparison of these measurements with simultaneous measurements obtained by use of a Joss–Waldvogel disdrometer. © 2006 Optical Society of America

OCIS codes: 100.0100, 010.3920, 100.2000.

1. Introduction

An important aspect of precipitation science is the measurement of the drop size distribution [DSD, denoted $N(D)$], which is the probability density function of raindrop size. The DSD, in addition to being a statistical quantity of fundamental interest, is related to other important quantities, such as rain rate R and mass density of falling rain M, according to the equations

$$R = (\pi/6)\int_0^\infty D^3 N(D) w_t(D) \mathrm{d}D, \tag{1}$$

$$M = (\pi\rho/6)\int_0^\infty N(D) D^3 \mathrm{d}D, \tag{2}$$

respectively. Here ρ is the density of water, $w_t(D)$ is the terminal velocity of the raindrop, and D is the raindrop's diameter. Precipitation radars are important and commonly used instruments for measuring rain rates over large areas, and the radar reflectivity factor Z is also related to the DSD by the equation

$$Z = \int_0^\infty N(D) D^6 \mathrm{d}D. \tag{3}$$

Further details of the interrelationships among the DSD, Z, and other aspects of radar measurement of precipitation can be found in Ref. 1.

Several methods exist for measuring the DSD. The most common of these is the Joss–Waldvogel disdrometer (JWD),[2] which consists of a Styrofoam cone with an exposed area of 50 cm^2, supported by an electromechanical unit. The amplitudes of voltage pulses created when raindrops impact the Styrofoam cone are used to infer the raindrop diameter. These diameters are stored in histogram bins that have a 0.3–5.5 mm diameter range. A sample DSD obtained with a JWD is presented in Fig. 1. One of the drawbacks of using the JWD concerns small drops. According to Tokay *et al.*,[3] the JWD underestimates the number of small drops during heavy rains. This underestimation occurs because of the recovery time required for oscillations of the Styrofoam cone to subside when the cone is hit by the drop. Additionally, the JWD often cannot differentiate between small drops and acoustic noise and therefore requires a

The authors are with the Department of Mechanical Engineering, Clemson University, Clemson, South Carolina 29634. J. R. Saylor's e-mail address is jrsaylor@ces.clemson.edu.

Received 24 June 2005; revised 31 October 2005; accepted 2 November 2005.

0003-6935/06/122672-17$15.00/0

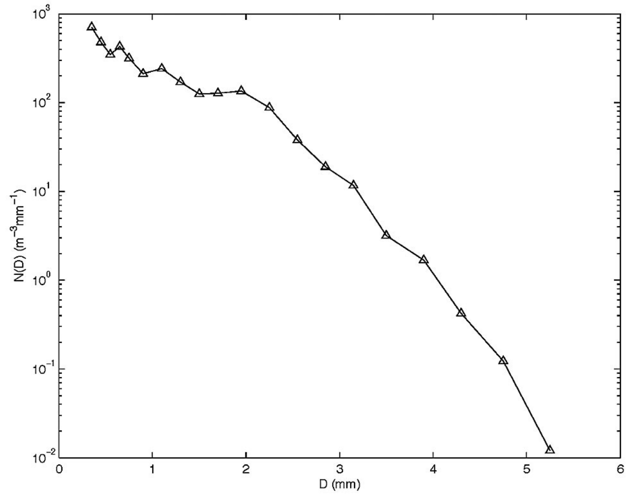

Fig. 1. DSD obtained with a JWD from rain during the 0th hour of July 1.

low-noise environment. Also, because the largest diameter recorded by the JWD is 5.5 mm, any (admittedly rare) drop larger than this is collected in the last bin. Finally, the JWD cannot measure the shape of a raindrop; this fact is important because use of dual-polarization precipitation radars to extract rain rate requires knowledge of both the DSD and the relationship between drop shape and drop diameter.[1] Specifically, the eccentricity e, given by

$$e = \{1 - \alpha^2\}^{1/2}, \tag{4}$$

is needed, where α is the ratio of the vertical to the horizontal extent of a drop:

$$\alpha = v/h. \tag{5}$$

Although equilibrium models for the shapes of raindrops exist,[4,5] they do not account for variations in the effective shape of the raindrop caused by drop oscillations, and the need for measurements of raindrop shape remains.

Another frequently used disdrometer, which is capable of obtaining drop shape, is the two-dimensional video disdrometer (2DVD).[6] This disdrometer consists of two line scan cameras located perpendicularly to each other, both of which obtain the image of the drop as it falls through a horizontal sheet of light. A matching algorithm is applied to the two scanned images to determine the size and shape of the raindrop. The 2DVD also has some shortcomings[3,7]: Because this disdrometer uses a scanning process, the drop image is affected by the horizontal velocity of the drop, resulting in a drop shape that appears more oblate or canted than is actually the case.[8] Additionally, the 2DVD often records extra raindrops because of splashing of the drops in the sensing area.

An emerging method that improves on existing techniques for measuring raindrop size and shape is direct optical imaging, in which the falling drop is

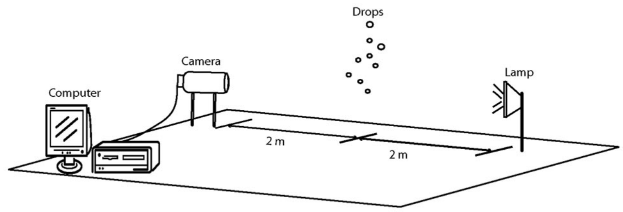

Fig. 2. Setup for obtaining raindrop images.

recorded with a CCD detector that images the entire drop at once, eliminating the problems associated with scanning instruments such as the 2DVD. A particularly useful setup for direct optical imaging is one in which the camera stares directly at a light source, imaging the silhouette of drops falling between it and the light source. This method of drop illumination has been used by NASA for rain measurement in a system referred to as the rain imaging system (RIS) developed by Bliven.[9] This system is used in the study reported here and is illustrated in Fig. 2. Earlier research on this system was conducted by Saylor *et al.*[7,10]

The general approach of illuminating a drop from behind is useful in drop imaging because it permits a well-defined depth of field. This is critical because conversion of a raindrop histogram into a DSD requires knowledge of the measurement volume, which is determined by the depth of field. Drop images obtained by use of the optical setup shown in Fig. 2 have the characteristic that those drops located in the focal region of the camera exhibit an image of the light source in the drop's center. This image of the source appears as a bright hole in the center of the drop's image. This feature can be conveniently used to differentiate in-focus and out-of-focus drops. Hence the presence of a hole in the image is used to quantify the depth of field as the distance along the optical axis for which the image exhibits a hole. Of course doing this requires conversion of the gray-scale image into a binary, or black-and-white, image. This is done by thresholding, in which all pixels greater than a threshold level are set to white and those less than the threshold are set to black. This thresholding process is shown in Fig. 3: A sample gray-scale raindrop image is presented in Fig. 3(a) and the binary version obtained with a thresholding method is presented in Fig. 3(b). Note that in Fig. 3 two of the drop images (identified by arrows) have holes and are therefore located within the depth of field. Several out-of-focus drops are also present in the gray-scale image; in the thresholded image these become solid black objects. An enlarged version of the two in-focus drops is shown in Fig. 4. Considering only those images that exhibit a hole in the drop's center provides an objective method for defining the depth of field. However, because the existence of a hole in the thresholded image is partially determined by the thresholding algorithm employed, the depth of field is a function of the thresholding algorithm.

A trade-off exists between depth of field and accu-

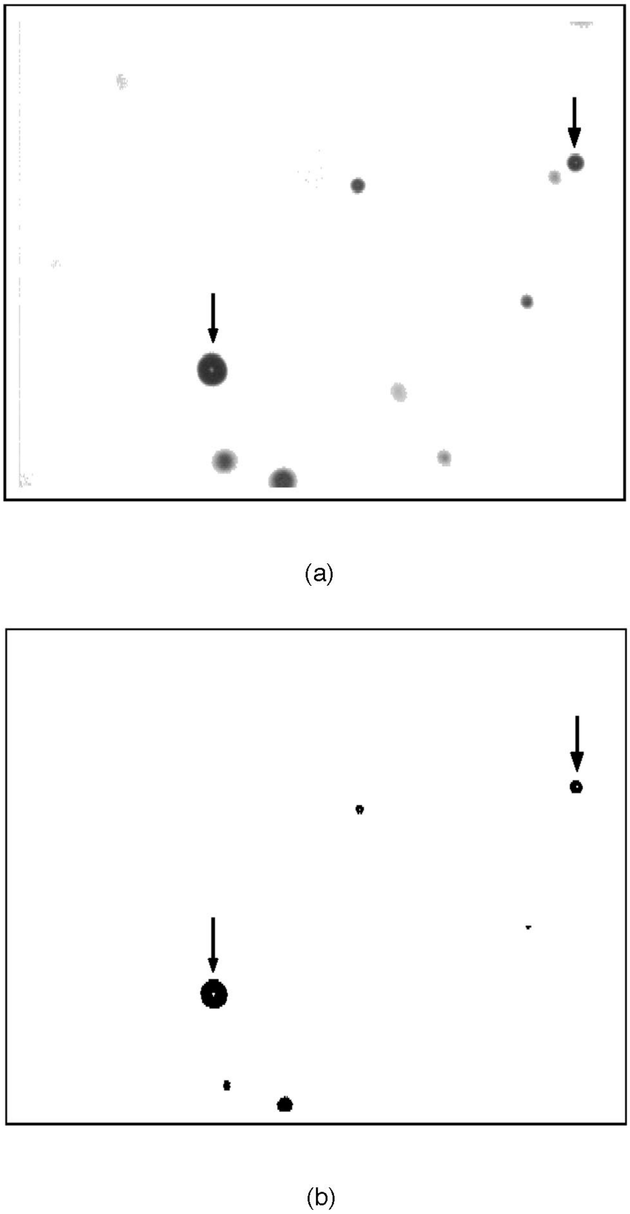

Fig. 3. (a) Sample gray-scale image frame. (b) Binary version of the image frame obtained with fixed thresholding. Drop images indicated by arrows are in focus.

racy in the optical system used here, as is the case with most optical imaging techniques. The size of the drop's image depends on the location of the drop along the optical axis. A drop closer to the camera appears larger than one farther away; i.e., it has a larger value of magnification ratio M, defined as

$$M = D_m/D, \tag{6}$$

where D_m is the drop diameter in the image and D is the actual drop diameter. One can decrease the variation in M, and hence increase the accuracy of the drop measurement, by reducing the depth of field. However, for the measurement of raindrops a small depth of field is problematic, as a large number of

Fig. 4. Magnified images of the two in-focus drops identified in Fig. 3(b).

drops are required for a statistically converged DSD to be obtained. This is an especially challenging requirement because the DSD can evolve within a given storm, increasing the need for obtaining a large number of drop measurements in a short period of time and hence the need for a large depth of field. As the depth of field and the drop diameter in the thresholded image are both functions of the thresholding algorithm, an investigation of how various thresholding algorithms affect these two quantities is needed. This is the objective of the study reported in the present paper.

Here we discuss the thresholding algorithms in some detail. The gray-scale images such as those in Fig. 3(a), obtained by use of the setup shown in Fig. 2, would ideally exhibit bimodal histograms, permitting a simple choice of the threshold as the minimum between the two peaks. Unfortunately the histograms for these raindrop images lack a clear global minimum or even a significant peak for the object (drop) pixels, as is shown in the sample histogram, presented in Fig. 5. In these images the hole in the center of the drop image does not have the same gray level as that of the background, and the boundary between the object and its hole is not easily defined. In addition, the number of background pixels is large,

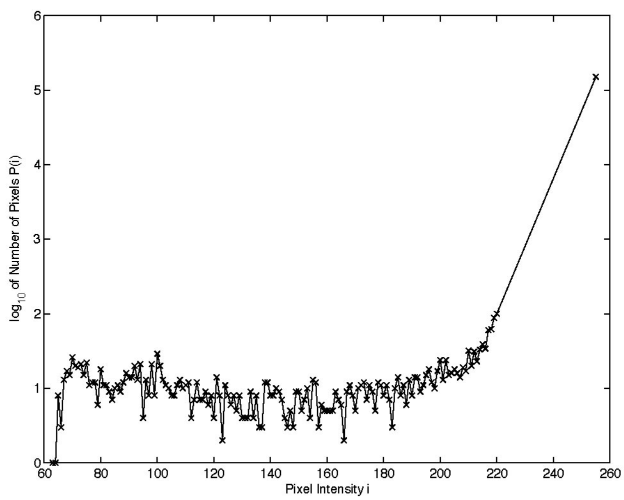

Fig. 5. Sample histogram of a raindrop image obtained with the setup in Fig. 2. Note that the large value at $i = 255$ corresponds to the background.

and this can affect some thresholding methods. Even if the $i = 255$ bin of the histogram is ignored, there is still no clear demarcation between the hole and the object pixels, making the choice of a threshold challenging. In this study we evaluated several thresholding methods to determine which provides the greatest depth of field with the least measurement error in drop diameter. As it was impossible to pursue all available thresholding algorithms, only those that occurred frequently in the literature were considered. This somewhat arbitrary list of algorithms is presented below, along with a brief description of each. The gray-scale images used in this work were 8 bit images, and a maximum gray level of 255 is assumed in the remaining discussion.

A. Fixed Thresholding

In the fixed thresholding method a fixed gray level is selected by the user. The pixels that have gray levels less than or equal to this value are set to black, and the remaining pixels are set to white. The value of the threshold is chosen by the user by trial and error, in which a trade-off is made between the quality of the binary image and the requirement for a reasonable value of depth of field. A value of 110 was found to work best here.

B. Iterative Thresholding

Iterative thresholding[11,12] begins with an approximate threshold that is successively refined to yield a final threshold, based on some property of the background and object regions. The steps below illustrate this algorithm as described by Leung and Lam[12]:

(a) An initial threshold value T is chosen. This is typically the average intensity of the image.

(b) The image is partitioned into two regions by use of current threshold T: object region R_o and background region R_b.

(c) Mean gray values μ_o and μ_b are calculated for these two regions:

$$\mu_0 = \sum_{i=0}^{T} ip(i), \tag{7}$$

$$\mu_b = \sum_{i=T+1}^{255} ip(i), \tag{8}$$

where $p(i)$ is the gray-level probability density function for the image.

(d) The new threshold is calculated as

$$T = (\mu_0 + \mu_b)/2. \tag{9}$$

(e) Steps (b)–(d) are repeated until two successive threshold values are the same.

C. Entropy Thresholding

Entropy thresholding[13] yields the threshold that maximizes the entropy of both the object and the background. For each threshold value T ranging from 0 to 255, the entropies for the object (H_o) and for the background (H_b) are calculated as

$$H_o = -\sum_{i=0}^{T} \frac{p(i)}{q_o(T)} \times \log \frac{p(i)}{q_o(T)}, \tag{10}$$

$$H_b = -\sum_{i=T+1}^{255} \frac{p(i)}{q_b(T)} \times \log \frac{p(i)}{q_b(T)}. \tag{11}$$

The functions $q_o(T)$ and $q_b(T)$ are the probabilities that a given pixel belongs to the object or the background, respectively, when the image is thresholded by use of T:

$$q_o(T) = \sum_{i=0}^{T} p(i), \tag{12}$$

$$q_b(T) = \sum_{i=T+1}^{255} p(i). \tag{13}$$

The threshold T is the value of i that maximizes $(H_o + H_b)$. Improved versions of this entropy thresholding method are also available.[14]

D. Double Thresholding

Double thresholding[11] is based on clustering pixels that are similar in gray values and are in close spatial proximity to one another. Following the development presented by Jain *et al.*,[11] the algorithm proceeds as follows:

(a) Two threshold values, T_1 and T_2 are selected. T_2 is selected by use of some other thresholding algorithm, and T_1 is generally taken as half of T_2.

(b) The image is segmented into three regions: R_1 is the object region, which contains the pixels with gray values less than T_1. These pixels are given one binary value. R_2 contains the pixels with gray values from T_1 to T_2. R_3 is the background region, which contains all the pixels with gray values above T_2. The pixels in this region are assigned the second binary value.

(c) The pixels in region R_2 are now assigned to R_1 or R_3 based on their positions in the image. Each pixel in R_2 that has any of its eight neighbors in R_1 is assigned to R_1; i.e., it is assigned a binary value that corresponds to R_1.

(d) The remaining pixels in region R_2 are assigned to region R_3.

For the current research the value of T_2 was obtained by the Ostu thresholding method,[15] and T_1 was set to half of T_2. As noted below, the Ostu method did not work particularly well as an independent thresholding method, but it did work well in the selection of T_2 for double thresholding.

E. Moment Preservation (MP)

In the method of moment preservation[16] the threshold values are computed such that the moments of the input image are preserved in the output binary image. Before thresholding, the kth moment of a gray-scale image, m_k, is calculated as

$$m_k = \sum_{i=0}^{255} p(i) i^k. \tag{14}$$

For each threshold value T ranging from 0 to 255, the gray-scale image is thresholded by use of T, and the kth moment of the binary image is calculated as

$$b_k = q_o(T)\mu_o(T)^k + q_b(T)\mu_b(T)^k, \tag{15}$$

where $q_o(T)$ and $q_b(T)$ are given by Eqs. (12) and (13), and $\mu_o(T)$ and $\mu_b(T)$ are given by Eqs. (7) and (8), respectively. The threshold T that preserves the values of the first k moments (typically up to the third) in the binary image is used as the threshold. This approach may be regarded as a moment-preserving image transformation that recovers an ideal image from a blurred version. In the present study we considered only the first two moments, the mean and the rms, when we used this method. By selecting a threshold that preserves the mean and the rms of the binary image we assumed that the object is recovered correctly.

Three other thresholding methods were considered in addition to the five described above. These were the Ostu method,[15,17] P-tile thresholding,[11] and the use of fuzzy sets.[18,19] However, these three methods failed to create a hole in the drop image even when the drop was located at the exact focal point of the camera. Hence these methods are not considered further here.

When the large number of images acquired during actual raindrop imaging are analyzed, occasional nonraindrop images are recorded. These arise from, for example, insects, leaves, and electrical noise in the video signal. We evaluated several ellipse detection methods to separate such images from the desired raindrop images. Among these methods were the symmetry detection techniques of Ho and Chen[20] and Lei and Wong,[21] the application of the Hough transform,[22] and the chord-tangent method.[22,23] Each of these methods had its strengths and weaknesses; however, they all required significant computational time. After some experimentation it was recognized that a simple algorithm that rejected objects based on the ratio of their vertical to horizontal extent worked just as well, with minimal computational expense. This ratio is identical to α defined in Eq. (5). Hence, for analysis of actual raindrop images we considered only those image objects for which $0.4 < \alpha < 1.2$. Existing research on raindrop image shape has revealed that actual raindrops do not exhibit α ratios outside this range.[4,24–26]

Another algorithm that is required for automatically processing the raindrop images acquired by the method considered here is the identification of a hole in the image object. Several hole detection algorithms available in the literature, such as the hit-or-miss method of Serra,[27] various lateral histogram and template matching algorithms,[22] and the normal vector method of Xia,[28] were evaluated. None of these hole detecting algorithms was found to be efficient in analyzing raindrop imagery, and a new hole detecting technique was developed: This method is a boundary counting method, which identifies objects that have two boundaries and classifies them as having a hole. This boundary counting algorithm is described briefly in Section 2 below.

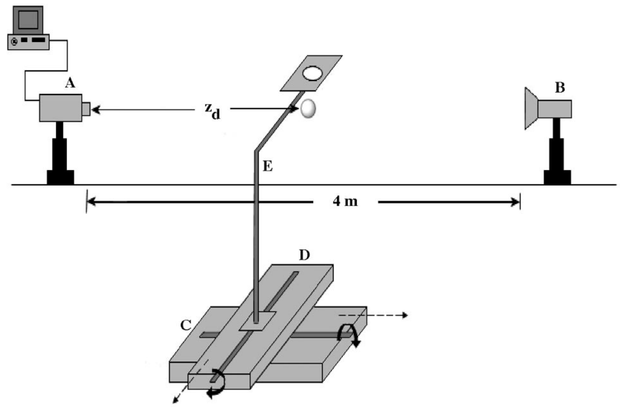

Fig. 6. Setup for obtaining laboratory data: A, CCD camera; B, lamp; C, translation stage along the optical axis (z axis); D, translation stage along the x axis; E, dropping arm.

To evaluate the thresholding algorithms described above, we performed laboratory experiments and field measurements. In the laboratory experiments, glass spheres of known diameter were imaged. These spheres ranged in diameter from 3 to 8 mm and were used to quantify the depth of field of the system for each thresholding method as well as to determine the accuracy in diameter measurement for each algorithm. As noted in Section 2, manufacturing difficulties prevented use of glass spheres of diameters smaller than 3 mm. Hence comparison of imagery-based rain quantities with JWD measurements required extrapolation of the laboratory data for diameters smaller than 3 mm. Field experiments were conducted in which raindrop imagery was obtained simultaneously with JWD measurements. DSDs and rain rates were computed from the imagery and compared with those obtained from the JWD. Analyses of the imagery by use of each of the thresholding methods described above permitted determination of the accuracy of each of these methods in computing the rain rate and the DSD.

2. Experimental Method

The laboratory apparatus used in this study is presented in Fig. 6. To quantify the measurement accuracy of the system, it was necessary to obtain images of drops of known diameter. Because of the difficulty associated with creating water drops that have a prescribed diameter, solid MgF_2 spheres were used instead. MgF_2 has a refractive index of $n = 1.37$, close to that of water ($n = 1.33$), providing a comparable simulation of a water drop.[29–31] We obtained images of MgF_2 spheres by dropping the spheres from the dropping arm at various locations along the optical axis, z_d. The height of the vertical bar was set such that it was just above the image frame; hence the spheres were imaged as soon as they were dropped. Saylor *et al.*[7] used a similar setup, in which the glass spheres imaged by the camera were mounted onto a metal post. Thus the spheres were stationary, and the frame contained the image of the post. This approach was not feasible here because the thresholding algorithms investigated here are sensitive to the number of object pixels, which is affected by the presence of the metal post in the image, a problem avoided by dropping the spheres through the imaged region. The dropping arm was supported by two translation stages [Velmex, Inc., 0.01 in. (0.025 cm) resolution], which permitted the x location (the horizontal direction in the image frame) and the z location (the direction of the optical axis) of the dropping position to be varied. MgF_2 spheres with diameters of 3, 4, 5, 6, 7, and 8 mm were investigated here. A diameter range extending to smaller values was desired because, as shown in Fig. 1, many raindrops have a diameter of less than 3 mm. However, manufacturing difficulties precluded the use of spheres smaller than those considered here.

The CCD camera had a 640 × 240 pixel detector, and the camera was focused at a location 200 cm from the camera, halfway between the lens and the halogen lamp. The camera was fitted with a 220 mm zoom lens. We fixed the camera's magnification by adjusting the zoom such that the frame size was 32 mm × 24 mm, resulting in pixel resolutions of 0.05 and 0.1 mm/pixel in the x and y dimensions, respectively. We obtained this setting by imaging a fine-scaled rule placed 200 cm from the camera. A PC with LabVIEW data acquisition software was used to acquire and store the image frames. The light source was a 300 W halogen lamp. A gel paper (Lee Filters; #129, heavy frost type) was placed in front of the lamp to provide uniform background illumination intensity. The lamp was aligned such that its center was located on the optical axis.

To measure the depth of field (dof), a sequence of MgF_2 sphere images was obtained by a procedure similar to the one used by Saylor *et al.*[7] with the exception that MgF_2 spheres, not ordinary glass spheres were used and that these were dropped instead of mounted. Each sphere was dropped at 1 cm intervals in the z dimension beginning and ending at approximately 185 and 220 cm, respectively, from the camera. The distance between the dropping position and the camera lens (z_d) was recorded for each image. This procedure was repeated for each of the six diameters considered. All five thresholding methods (fixed thresholding, double, iterative, moment preservation, and entropy) were applied to each image obtained with the above procedure, followed by application of the boundary counting algorithm to detect holes. For each thresholded image, the measured diameter was computed as

$$D_m = \left(\frac{4A}{\pi}\right)^{1/2}, \tag{16}$$

with area A (in square millimeters) calculated as

$$A = P \times 0.1 \times 0.05, \tag{17}$$

where P is the total number of pixels in a thresholded sphere image (including the number of hole pixels, if present) and 0.1 mm × 0.05 mm is the area of one pixel.

The dof is defined as the difference between the value of z_d at which the hole first appears, z_s, and the value of z_d at which the hole disappears, z_e. Thus the dof is defined as

$$\mathrm{dof} = z_e - z_s. \tag{18}$$

Figure 7 shows gray-scale images of a 3 mm sphere taken at several z_d locations and their corresponding thresholded versions, obtained from each of the five thresholding algorithms. As the gray-scale images of this figure indicate, the sphere image is blurred when it is nearer the camera (e.g., z_d = 186 cm) and becomes sharper as it moves toward the focal point (z_d = 200 cm). A hole is observed in the focal region, signifying that the image is in focus. As the image is moved farther from the camera, it again loses focus and becomes blurry. The binary images show where the dof begins and ends for each algorithm. For example, the double thresholding image does not have a hole at z_d = 196 cm, but one is present at z_d = 198 cm. Hence, z_s for double thresholding is somewhere from 196 to 198 cm. Similarly, z_e for double thresholding is expected to be in the range z_d = 203–206 cm. A finer separation in z_d = 1 mm was used near these transitions to yield more precise measures of z_s and z_e.

The values of z_s and z_e also changed with the sphere diameter. For example, for a 3 mm sphere z_e is between 200 and 203 cm when entropy thresholding is used, whereas for an 8 mm sphere it is between 206 and 209 cm. These results are presented in detail in Section 3 below.

It is noted that, because the spheres were dropped, the location of the sphere in the image was random. We made a study to see whether the dof or the measured sphere diameter varied with the x and y locations in the image, but no significant variation was found.

The boundary counting algorithm was used to identify holes. This method utilizes the fact that an image object that has a single hole will have only two boundaries, one external and one internal. Before the number of boundaries is counted, however, a single object must be identified and separated from other objects in the image (for the case of multiple raindrops in one frame). To achieve this separation, the queue-based approach for region growing is used.[32] After the object is extracted, the following steps are performed to achieve hole detection:

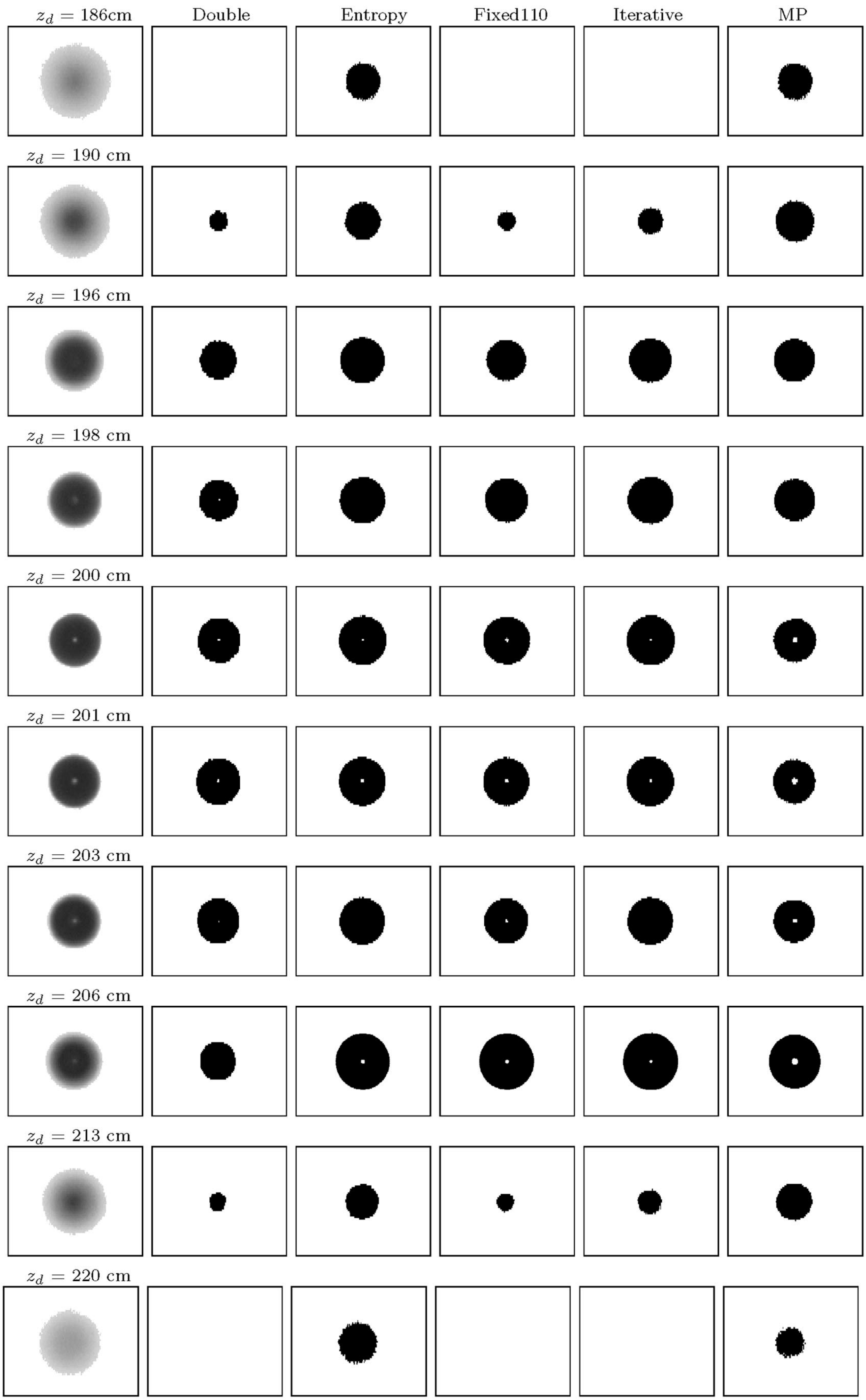

Fig. 7. Gray scale (leftmost column) and binary images of a 3 mm sphere.

(a) The boundary pixels that are four-connected to the object pixels are marked.

(b) The boundary following algorithm of Jain *et al.*[11] is applied to a selected marked pixel, from which it traverses the eight-connected marked pixels. The traversal is completed when the starting pixel from which the traversing was started is revisited.

(c) Step (b) is repeated until all the marked pixels are traversed. A counter is kept to record the number of times step (b) is performed, indicating the number of boundaries present in the object image. If the count is 2, the object contains a single hole and the drop is accepted as an in-focus drop. Any other value of this count results in the rejection of the object as having no hole.

Boundaries with rough edges affect the boundary following algorithm[11] and may result in an incorrect count of boundaries. One can address this problem by smoothing the object boundary before applying the boundary counting algorithm. For some of the work described herein, we tested smoothing by using either the morphological closing of Haralick *et al.*[33] or the boundary smoothing algorithm given by Yu and Yan.[34]

Field data consisting of raindrop images were obtained by use of the setup shown in Fig. 2, which was placed at the Clemson Atmospheric Research Laboratory in Clemson, S.C. Gray-scale imagery obtained during storms was processed by the hole detection algorithm described above, followed by the thresholding algorithms. We used these data to obtain the DSD and the rain rate for each hour of imagery recorded. This DSD was then compared with the DSD obtained from a JWD for the same hour. The JWD was used as obtained from the manufacturer; the manufacturer's calibration was used. The DSD was calculated as

$$N(D_k) = \frac{H(D_k)}{R_v \times l}, \tag{19}$$

where diameter $D_k = k \times 0.05$, bin size l is 0.05 mm, k is the bin number ($1 \leq k \leq 640$), $H(D_k)$ is the number of drops in bin k, and the measurement volume R_v is (in cubic millimeters)

$$R_v = (h - D_k) \times (w - D_k) \times (\mathrm{dof} - D_k) \times N_f. \tag{20}$$

The variable N_f is the total number of image frames from an hour's data. Multiplying N_f by the measurement volume gives the total volume sampled. Variables h, w, and dof are the height, width, and depth of field, respectively, of the measurement volume of the system. The height and width of the measurement volume are $h = 24$ mm and $w = 32$ mm. Although h and w of the frame change with z, the optical axis, this change inside the depth of field is less than 2 mm. The dof was calculated from the results of the laboratory data presented above. Note that in Eq. (20) D_k is subtracted from h, w, and the dof in computing R_v because drop images that intersect the edge of the frame were rejected, reducing the effective measurement volume used in the calculation.

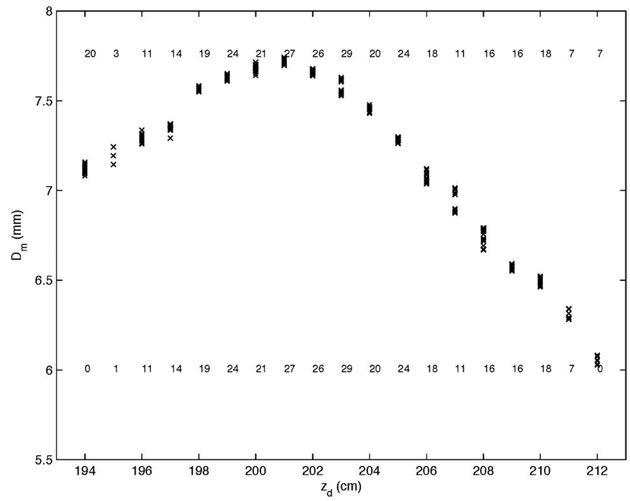

Fig. 8. Sample plot of measured diameter D_m versus z_d for an 8 mm sphere obtained by double thresholding. Each cross (×) represents a sphere image with diameter D_m and z position z_d. The numbers at the top are the total count of sphere images (n_t), and the numbers below are the count of sphere images with holes (n_h).

It should be noted that images such as those shown in Fig. 3(a) are not precisely those recorded by the camera. To store the video frames in a compressed format we applied a prethresholding algorithm to each image, which set to 255 the value of each pixel that has a gray value above 220. The value of 220 was chosen because, when no drops were in the field of view, the image histogram showed no values below this threshold. Hence any gray level less than 220 is due to an object in the field of view, and everything above 220 is background.

3. Results

A. Laboratory Data

A sample plot of measured diameter D_m versus z_d obtained from the images of the 8 mm sphere taken at 1 cm intervals of z_d and thresholded by the double thresholding method is shown in Fig. 8. The numbers above the points in this plot correspond to the total number of sphere images (n_t) acquired at that z_d, and the numbers at the bottom of the points correspond to the number of sphere images with a single hole (n_h). This plot shows that z_s lies somewhere in the range 194–196 cm because none of the sphere images has a hole at the former ($n_h = 0$) whereas at the latter all the images have holes. Similarly, z_s lies somewhere in the range 211–212 cm. Hence dof for the double thresholding algorithm applied to an 8 mm drop (sphere) is approximately 16 cm. To obtain a more precise value, we obtained images in the transitional region at 1 mm intervals. We obtained the exact values of z_s and z_e in these transitional regions by first computing the ratio $r = n_h/n_t$ in these regions and then fitting a straight line to the r-versus-z_d data; z_s and z_e were defined as the values of z_d for which this line gave $r = 0$.

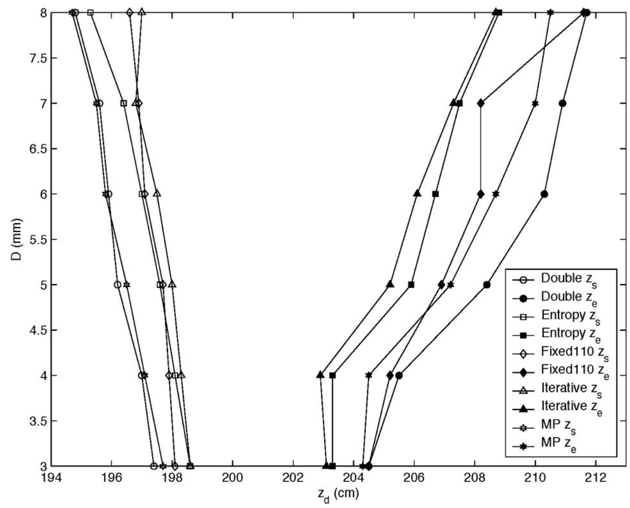

Fig. 9. All calculated z_e and z_s values for each sphere and each thresholding algorithm.

The resultant values of z_s and z_e for each sphere diameter and each thresholding algorithm are presented in Fig. 9. The dof obtained by subtracting z_s from z_e is plotted in Fig. 10. The data in this figure were fitted to a line of the form

$$\mathrm{dof} = sD + i. \tag{21}$$

These lines are included in Fig. 10, and the values of s and i and the 95% confidence level C_{95} for each fit are presented in Table 1. Figure 10 shows that the largest depth of field is achieved with the double thresholding algorithm; and the smallest, with the iterative thresholding algorithm. This is true for all diameters investigated. Ideally, the depth of field would be large and insensitive to diameter. However, Fig. 10 shows that, as expected, the depth of field increases with diameter for all thresholding algorithms considered and that this increase is linear in diameter. This sensitivity to diameter is smallest for the fixed thresholding method, as evidenced by the value of s in Table 1. The fixed thresholding algorithm also showed the least amount of scatter in the value of dof computed from the multiple images considered for each diameter, giving a value of $C_{95} = \pm 0.66$ cm for the fit.

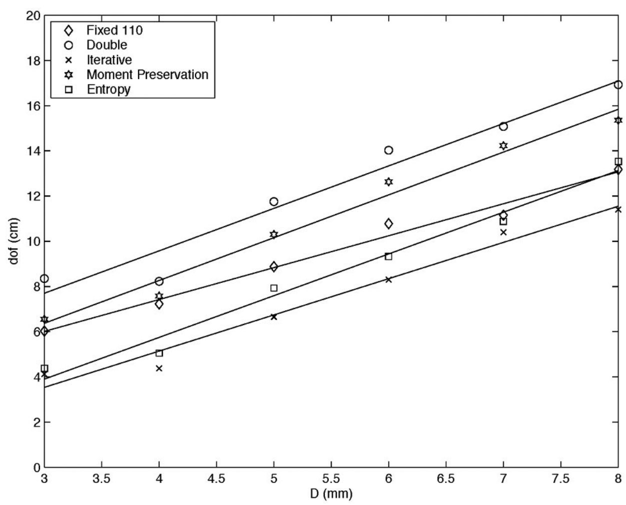

Fig. 10. Variation of dof with D for all thresholding algorithms.

Table 1. Slope and Intercept of the Lines Shown in Fig. 10 and 95% Confidence Level of the Linear Fit Presented in Eq. (21)

Thresholding Algorithm	Slope s (cm mm^{-1})	Intercept i (cm)	95% Confidence Level C_{95} (cm)
Double	1.88	2.07	±1.55
Entropy	1.85	−1.64	±0.95
Fixed 110	1.41	1.77	±0.66
Iterative	1.60	−1.27	±1.01
MP	1.89	0.70	±0.91

Figure 9 shows that the center of the dof shifts to the right (away from the camera) as the diameter increases, indicating that the dof is not symmetric about the focal point of $z_d = 200$ cm. This phenomenon can also be observed in the gray-scale images presented in Fig. 7, which shows that images remain sharper for a larger range of z_d when the sphere is moved away from the camera than when it is moved toward the camera.

Equation (21) and Table 1 can be used to obtain dof for a given D and a given thresholding method. However, because D is the actual diameter, not the measured diameter D_m, a mapping from D_m to D is needed. Figure 8 shows that D_m varies with z_d. Thus, for a given raindrop image, because the value of z_d is unknown it is impossible to determine the precise diameter D of the drop. To obtain D from D_m we averaged the values of D_m over the depth of field for each diameter and each thresholding algorithm. This procedure provided a mapping from D_m to D; of course it incurs an error because, for example, in Fig. 8 D_m ranges from 6 to 7.6 mm while D is 8 mm. Hence, for a raindrop with $D = 8$ mm, the measured value will be anywhere between these two values. This error is a necessary consequence of this finite depth of field imaging method.

To obtain the mapping between D and D_m we fitted a fourth-order polynomial to the D_m-versus-z_d data, and an average value for D_m was calculated as

$$\langle D_m \rangle = \frac{1}{\mathrm{dof}} \int_{z_s}^{z_e} F(D_m) \mathrm{d}D_m, \tag{22}$$

where $F(D_m)$ was the fourth-order polynomial fit. This averaging was done for each sphere diameter and thresholding algorithm. An example of this fit is shown in Fig. 11. The resultant $\langle D_m \rangle$-to-D mapping is presented in Fig. 12 for each thresholding algorithm, including the linear fit:

$$D = \frac{\langle D_m \rangle - i'}{s'}, \tag{23}$$

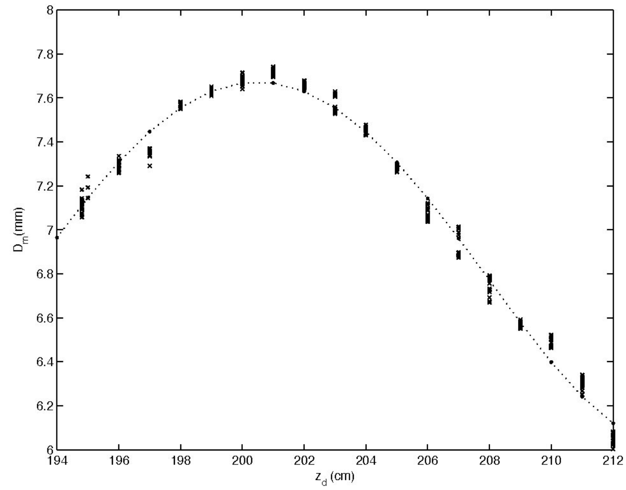

Fig. 11. Variation of measured diameter D_m within the depth of field for the 8 mm sphere obtained from double thresholding. The dotted curve is the fourth-order polynomial fitted to all the data points. A value of $\langle D_m \rangle = 7.17$ mm was obtained from Eq. (22).

where s' and i' are the slope and the intercept, respectively. The 95% confidence levels for the fitted lines were less than ± 0.1 mm. Table 2 lists the slopes and the intercepts of the lines fitted to the data. This mapping served two purposes, first to obtain D from D_m and second to obtain the dof from D by use of Eq.

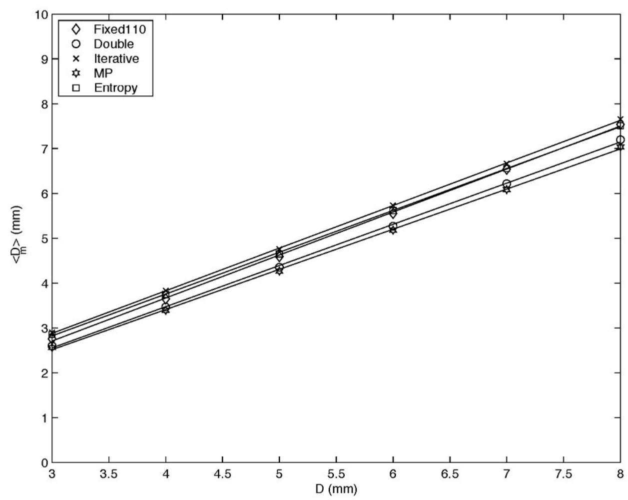

Fig. 12. Variation of $\langle D_m \rangle$ with D for all thresholding algorithms and each sphere diameter.

Table 2. Slope and Intercept of the Lines Shown in Fig. 12

Thresholding Algorithm	Slope s'	Intercept i' (mm)
Double	0.92	−0.20
Entropy	0.93	0.02
Fixed 110	0.96	−0.17
Iterative	0.95	0.03
MP	0.90	−0.17

Table 3. Tabulation of $\langle D_m \rangle$, D_b, σ_1, and σ_2 for Each D Investigated[a]

Algorithm	D (mm)	$\langle D_m \rangle$ (mm)	D_b (mm)	σ_1 (mm)	σ_2 (mm)
Double	3	2.6056	0.3944	0.1030	0.0255
	4	3.4401	0.5599	0.1512	0.0273
	5	4.3410	0.6590	0.2472	0.0380
	6	5.2543	0.7457	0.3415	0.0464
	7	6.2177	0.7823	0.3746	0.0506
	8	7.2049	0.7951	0.4490	0.0460
Entropy	3	2.8488	0.1512	0.0410	0.0799
	4	3.7410	0.2590	0.0675	0.0269
	5	4.6521	0.3479	0.1082	0.0905
	6	5.6078	0.3922	0.1309	0.1057
	7	6.5519	0.4481	0.1517	0.0384
	8	7.5106	0.4894	0.1937	0.2511
Fixed 110	3	2.7562	0.2438	0.0708	0.0184
	4	3.6502	0.3498	0.1188	0.0240
	5	4.5831	0.4169	0.1763	0.0244
	6	5.5543	0.4457	0.2261	0.0313
	7	6.5437	0.4563	0.2224	0.0350
	8	7.5404	0.4596	0.2915	0.1547
Iterative	3	2.8888	0.1112	0.0426	0.0134
	4	3.8185	0.1815	0.0647	0.0167
	5	4.7480	0.2520	0.1133	0.0202
	6	5.7282	0.2718	0.1290	0.0212
	7	6.6682	0.3318	0.1633	0.0313
	8	7.6453	0.3547	0.2536	0.1520
Moment Preservation	3	2.5607	0.4393	0.0241	0.0201
	4	3.3953	0.6047	0.0516	0.0224
	5	4.2620	0.7380	0.0741	0.0712
	6	5.1722	0.8278	0.1268	0.3276
	7	6.0843	0.9157	0.1581	0.0992
	8	7.0065	0.9935	0.1745	0.3389

[a]A set of these statistics is presented for each algorithm explored.

(21). This mapping was needed when we analyzed the field data to compute the DSDs and rain rates.

For all algorithms listed in Table 2, the slope s' is less than unity, meaning that the measured diameter is always less than the actual diameter. Ideally, a slope as close to unity as possible is desired. The algorithm that provides the value of s' closest to unity is the fixed thresholding method ($s' = 0.96$). Of course, as long as this slope is known, D can still be obtained from D_m.

The values of $\langle D_m \rangle$ for each D investigated obtained with each of the five algorithms are presented in Table 3. Along with this average value are presented the bias, $D_b = D - \langle D_m \rangle$, and two standard deviations, σ_1 and σ_2. σ_1 is the standard deviation of the fourth-order curve fit (like that shown in Fig. 11) from its own average, and σ_2 is the standard deviation of the individual D_m points from the fourth-order curve fit.

B. Field Data

Fifteen hours of rain data were recorded, processed, and their corresponding DSDs and rain rates obtained. Figure 13 shows one such DSD obtained during the 0th hour (12:00 midnight–1:00 AM) of 1 July 2004. In this figure, DSDs obtained with each thresh-

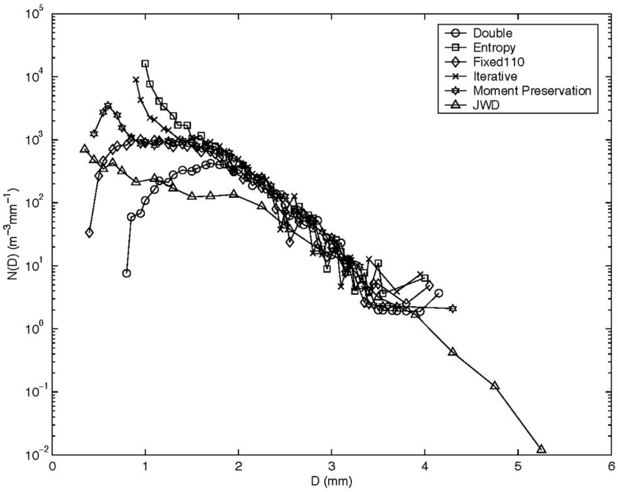

Fig. 13. DSDs of the rain that occurred during the 0th hour of 1 July obtained from all the algorithms and the JWD.

olding algorithm are presented, along with the DSD obtained by use of the JWD.

The rain rate R (in millimeters per hour) for the hour was calculated from

$$R = \frac{\pi}{6} \sum_{k=1}^{640} {D_k}^3 \times N(D_k) \times w_t(D_k) \times 0.05, \qquad (24)$$

where k is the bin number for diameter $D_k = k \times 0.05$ (0.05 mm is the bin width), $N(D_k)$ is the DSD value that corresponds to D_k, and the terminal velocity $w_t(D)$ is

$$w_t(D_k) = 9.65 - 10.3 \times \exp(-600 \times D_k), \qquad (25)$$

a relation obtained by Atlas *et al.*[35] Here $w_t(D)$ is in units of meters per second and D_k is in meters. The rain rates that correspond to the DSDs obtained for each of the 15 h of recorded rainfall are presented in Table 4. The DSD for each of these 15 hours shows characteristics similar to those shown in Fig. 13 and are not presented here because of space limitations. Significant variations are observed from algorithm to algorithm and also between any one algorithm and the JWD. It should be noted that on these semilog plots the JWD DSD is a relatively straight line, indicating a pure exponential distribution, while the DSDs obtained from the imagery all exhibit some finite amount of curvature. This seems to indicate that a better model for the DSDs obtained from the imagery is the gamma distribution described by Ulbrich,[36] rather than the simple exponential distribution.

The DSDs presented in Fig. 13 show that the DSD obtained from the JWD lies below the DSDs obtained from the algorithms, especially for $D < 3$ mm. Also, the JWD has recorded drops with diameters greater than 4.5 mm. Because the DSD values for the algorithms are greater than the DSD values for the JWD, R obtained from the algorithms is higher than R obtained from the JWD. One might expect that, as the JWD recorded drops of larger diameter and because larger diameters contribute more to R, the JWD should give a greater R. Overall, however, the number of large diameter drops is small and contributes little to R. For the JWD DSD shown in Fig. 13, the contribution of DSD values for $D > 4$ mm to R is only 0.127 mm h^{-1}, accounting for a mere 0.65% of the total R. Figure 13 shows that, other than the extension of the JWD DSD into the large diameter region, all the plots almost coincide for $D > 3$ mm; thus the difference in R is due primarily to variations in the DSDs for $D < 3$ mm. The algorithms that have lower $N(D)$ values in this region have a lower R. For the DSD presented in Fig. 13 the double thresholding algorithm gives the lowest R, while entropy thresholding gives the highest. This is also true

Table 4. Rain Rates (mm h^{-1}) Obtained for Each of the 15 h of Recorded Rain Data[a]

		Algorithm					
Hour	Date, Rain Hour Processed	Double	Entropy	Fixed 110	Iterative	MP	JWD
1	28 July, 1st hour	34.565	62.312	41.986	52.691	49.724	28.925
2	25 June, 20th hour	25.595	56.997	34.114	45.323	41.666	20.534
3	27 July, 1st hour	23.762	45.974	29.236	31.231	37.232	20.085
4	1 July, 0th hour	25.296	52.640	31.282	44.874	37.743	19.594
5	25 June, 12th hour	20.229	46.677	27.995	45.845	34.179	17.601
6	28 July, 0th hour	19.344	35.754	22.514	30.854	24.401	13.596
7	25 June, 22nd hour	17.161	29.520	19.315	23.812	24.355	10.933
8	27 July, 0th hour	10.325	27.245	14.432	19.081	18.917	10.293
9	14 June, 19th hour	13.832	32.229	17.227	22.890	22.180	8.735
10	14 June, 18th hour	8.849	18.233	10.758	12.396	13.665	7.238
11	13 July, 18th hour	8.626	20.653	10.881	19.273	13.281	6.596
12	4 July, 15th hour	5.600	14.291	7.210	9.831	9.834	5.070
13	1 July, 19th hour	2.869	9.132	3.891	4.558	5.688	3.239
14	30 June, 12th hour	1.393	4.860	2.172	4.332	3.427	1.658
15	30 June, 23rd hour	2.646	7.174	3.771	5.160	5.161	0.917

[a]All the hours of rain data are from the year 2004; 0th hour is midnight to 1 a.m.

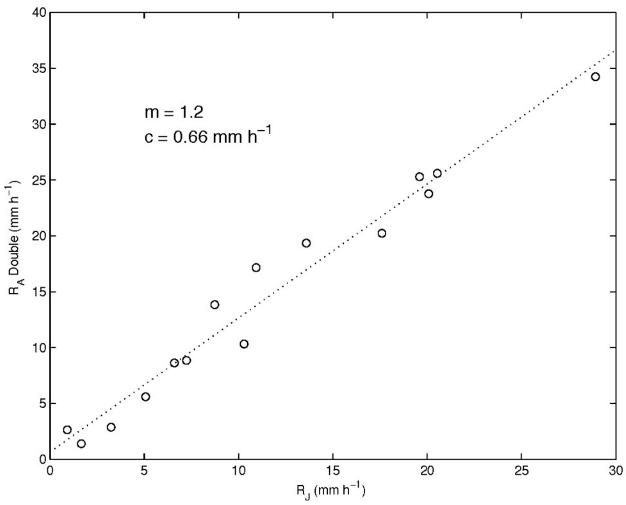

Fig. 14. R_A from the double thresholding algorithm versus R_J.

Table 5. Parameters Relevant to the Linear Fits of R_A to R_J in Figs. 14 and 15

Thresholding Algorithm	Slope (m)	Intercept c (mm h^{-1})	95% Confidence Interval (mm h^{-1})	Correlation Coefficient
Double	1.20	0.66	±3.15	0.984
Entropy	2.24	4.78	±7.16	0.976
Fixed 110	1.50	0.98	±3.19	0.989
Iterative	1.92	2.42	±8.70	0.954
MP	1.77	2.17	±4.05	0.988

for each of the 15 h of rain rate data presented in Table 4.

Plots of R calculated with a thresholding algorithm, R_A versus R obtained from the JWD, R_J, are presented in Figs. 14 and 15. Figure 14 shows the plot of R_A versus R_J for the double thresholding algorithm, which shows the best agreement with the JWD data.

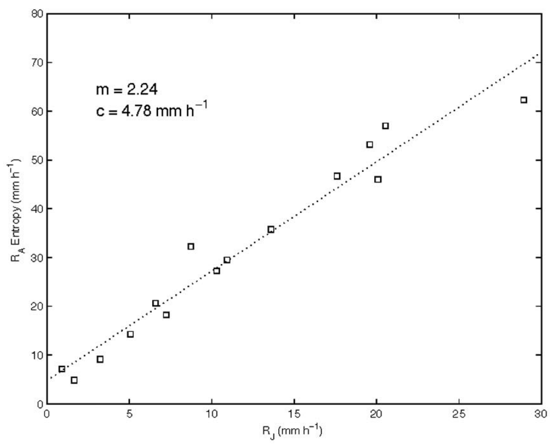

(a) Entropy

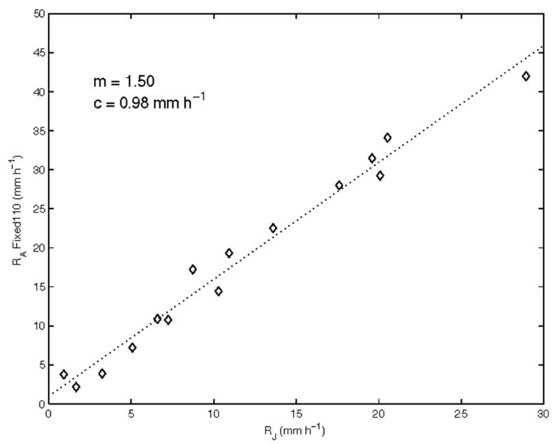

(b) Fixed110

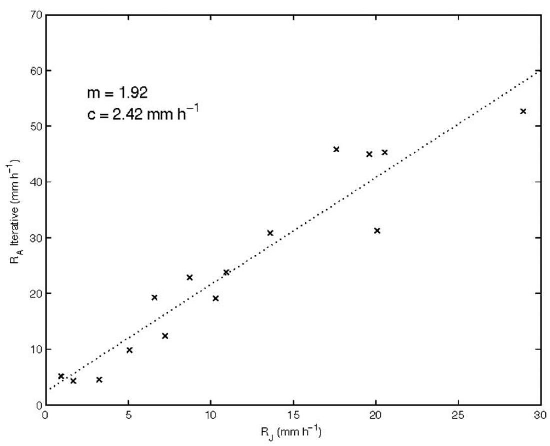

(c) Iterative

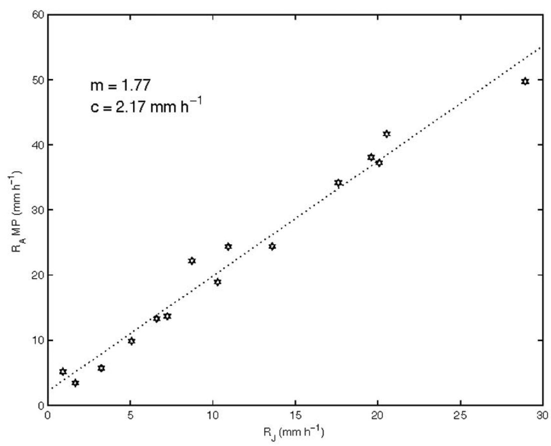

(d) MP

Fig. 15. R_A versus R_J for four of the thresholding algorithms.

Plots for the remaining algorithms are presented in Fig. 15. A line fitted to the data points is presented in each plot, which has the form

$$R_J = \frac{R_A - c}{m}\,[\mathrm{mm\ hr}^{-1}], \tag{26}$$

and values of m and c for this equation are presented in Table 5 along with the error in the fit. The values of R_A and R_A are well correlated in Figs. 14 and 15 as evidenced by the correlation coefficients presented in Table 5, defined as

$$\gamma = \frac{\langle R_A R_J\rangle - \langle R_A\rangle\langle R_J\rangle}{\sigma_A \sigma_J}, \tag{27}$$

where $\langle\ \rangle$ signifies averaging and σ_A and σ_J are the standard deviations of R_A and R_J, respectively.

The data in Tables 4 and 5 show that the entropy and iterative algorithms give approximately twice the values of R than the JWD. The double thresholding method gives values for R closest to those of the JWD and also has the smallest error in fitting, defined here as the 95% confidence interval for the linear fit to the data. The entropy and iterative thresholding methods show a larger amount of error in fitting.

4. Discussion

An evaluation of the results obtained by use of thresholding algorithms is complicated by the fact that no truly standardized method of rain measurement exists. All rain measurement devices suffer from a variety of error sources, many of which are difficult to quantify. Here we compare the algorithmic results obtained with the results from the JWD. This is a necessarily less than accurate process because it is known that the JWD itself has inherent measurement errors. Hence we simply point out differences between the two devices. The algorithmic measurement of the DSD and the rain rate has several errors that can be quantified, and these are described below.

An important result of this work is revealed in Figs. 14 and 15, which show that the relationship between R obtained from the algorithms and R obtained from the JWD is highly linear. Hence, if the goal is to measure rain rate, and if the JWD is presumed to provide an accurate rain rate measurement, the optical method presented herein can easily be mapped by use of Eq. (26) to a correct rain rate.

The major source of error in the rain measurement method investigated here is in the mapping between D and D_m given by Eq. (23). Figure 12 shows the mapping of the image diameter to the actual diameter for each of the thresholding algorithms. We achieved this mapping by computing the average values of D_m, using Eq. (22). However, the value attained by D_m, for a given D, varies significantly with z_d. As exhibited in Fig. 11, the variation in measured diameter is large for a given drop size over the depth of field of the camera. This is shown more clearly in Fig. 16, which shows the mapping by the double thresholding method for a given measured drop diameter of 3.6 mm. The upper (dotted) line shows the minimum possible actual drop diameter (3.78 mm), and the lower (dashed) line shows the maximum possible actual drop diameter (4.63 mm). During actual analysis of raindrop data by this algorithm, a measured drop diameter of 3.6 mm would be mapped to an actual value of 4.03 mm. However, the true actual value could reside anywhere from 3.78 to 4.63 mm. Additionally, the mapping between D and D_m for diameters less than 3 mm is extrapolated, as we acquired data by using MgF_2 spheres only down to a diameter of 3 mm. Additional errors may be incurred if the linear D and D_m relationship is altered in this small diameter range. Behavior similar to that of Fig. 16 is observed for the other thresholding algorithms.

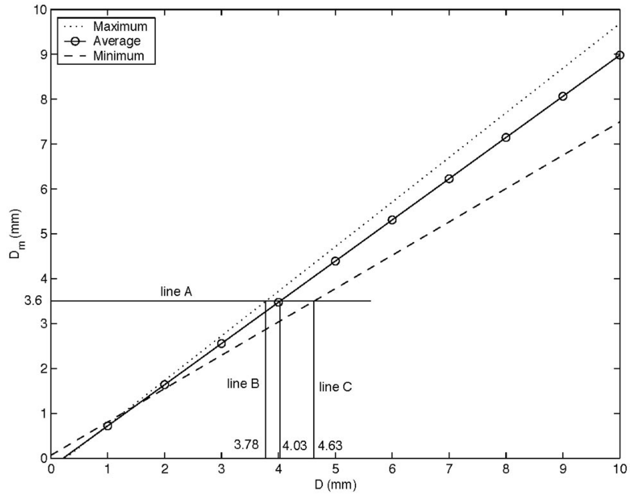

Fig. 16. Mapping of D_m to D for double thresholding. Solid line, mapping corresponding to the average value; i.e., for a given D_m on average, the actual diameter D will be obtained from this line. The dotted and dashed lines are the fitted lines for the maximum and minimum values of D_m, respectively.

As noted above, this error does not significantly influence the ability of this method to reproduce rain rates measured by a JWD. However, this error does affect the DSD. The range in possible actual drop diameters that correspond to the measured diameters, described above, results in misclassification of drop diameters in DSD bins. This effect is shown in Fig. 17, where we have plotted the DSD for a single hour of rain obtained from the double thresholding algorithm, using the D to D_m mapping, as well as the maximum and minimum bounds on this mapping illustrated in Fig. 16. Hence the DSDs that are obtained result in some misclassification of drops, although drops of a given diameter are, on the average, correctly classified. This process results in a DSD that is effectively a blurred version of the maximum and minimum DSDs presented in Fig. 17.

It should be noted that errors that are due to mapping are not inherent in the algorithms but rather are

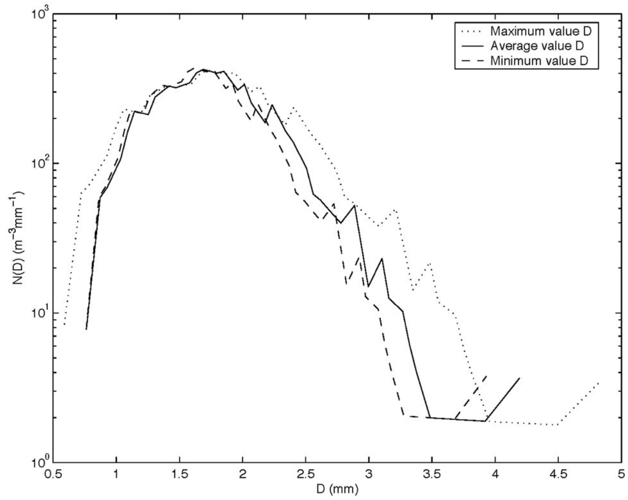

Fig. 17. DSD for the rain that occurred during the 0th hour of 1 July obtained from double thresholding when the D_m-to-D mapping was changed. Dotted curve, the DSD obtained when D_m was mapped to the maximum value that D can take. Dashed curve, DSD obtained when D_m was mapped to the minimum value.

due to the finite dof of the imaging systems. Reduction in dof either by selection of a thresholding algorithm that has a small dof or simply by changing the camera's $f/\#$ would increase the accuracy of the DSD. However, this would be done at the price of reduced measurement volume.

The data presented in Fig. 8 show how the number of holes present in the recorded images of MgF_2 spheres changes with distance from the focal point of the camera. Detailed investigation of many of these images showed that, outside the depth of field, some drop images were quantified by the boundary counting algorithm as having a hole. This typically occurred for very blurry images that, once thresholded, resulted in a rough boundary. The boundary counting algorithm would detect two boundaries in some of these out-of-focus images and accept them as in focus. Although this occurred to some extent for all the thresholding methods, it was particularly true for the entropy and MP methods because these two algorithms always select a threshold value between the minimum and the maximum gray levels of the image. Thus, for a very blurry image for which the minimum

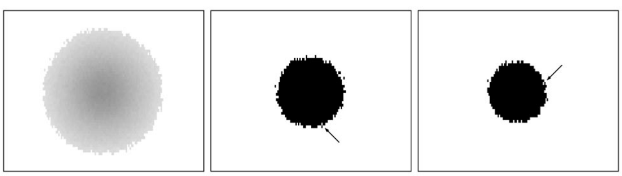

(a) $z_d = 185$ cm (b) Entropy (c) MP

Fig. 18. Gray-scale and binary images from entropy and MP thresholding algorithms of a 3 mm sphere at $z_d = 185$ cm. Note that the gray-scale image is very blurry and should be rejected. The binary images show the presence of a small hole near the boundary of the image. These images were wrongly accepted as in-focus images.

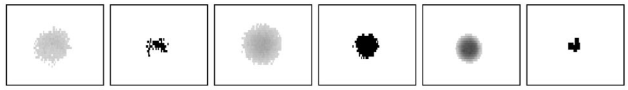

(a) (b) (c)

Fig. 19. Examples of out-of-focus drops selected as in focus. (a) MP thresholding, $D = 0.59$ mm; (b) entropy thresholding, $D = 1.04$ mm; (c) double thresholding, $D = 0.50$ mm.

gray value was close to 255, these two algorithms always gave a threshold above this level, resulting in a nonzero count of object pixels, whereas the other methods typically returned a blank frame. An example of this behavior is shown in Fig. 18 for entropy and MP thresholding for the 3 mm MgF_2 sphere. Both of these images were accepted as in-focus images owing to the presence of a small hole (of 1 pixel) near the boundary. This problem was also found in field data, examples of which are presented in Fig. 19.

When field data are analyzed, this misclassification phenomenon results in an overestimation of the in-focus drops and usually classifies these drops in the wrong DSD bin. This problem is part of the reason why the DSDs obtained from algorithms lie above the DSDs obtained from the JWD for much of the diameter range.

Prominent differences between the DSDs occur at $D \leq 3$ mm, and images in this diameter range were examined manually. For the rain that occurred during the 0th hour of July 1, the in-focus drops lying in diameter ranges 0.4–0.6, 0.9–1.1, 1.4–1.6, 1.9–2.1, and 2.9–3.1 mm were manually inspected for errors in the drop images. The number of accepted drops examined for each diameter range is presented as $H(D)$ in Table 6, along with the number of incorrectly accepted drops, $H_o(D)$. It was found that most of the smaller drops did not have holes but were accepted by the boundary counting algorithm; this was due either to rough boundaries with deep notches or to the presence of a one pixel hole near the boundary. Examples of these types of incorrectly accepted image are shown in Fig. 19.

The error in acceptance of out-of-focus drops was quantified as

$$E_p(D) = \frac{H_o(D)}{H(D)} \times 100 \tag{28}$$

Table 6. Total Number of Examined Drops Accepted as In Focus $H(D)$ and Number of Out-of-Focus Drops Incorrectly Accepted $H_o(D)$ for Each Thresholding Algorithm and Each Diameter Range

Diameter Range (mm)	$H(D)$	$H_o(D)$ for Thresholding Algorithm: Double	Entropy	Fixed 110	Iterative	MP
0.4–0.6	60	59	59	56	60	60
0.9–1.1	50	29	49	14	35	33
1.4–1.6	40	0	26	2	10	12
1.9–2.1	30	0	4	2	3	6
2.9–3.1	20	0	0	0	0	0

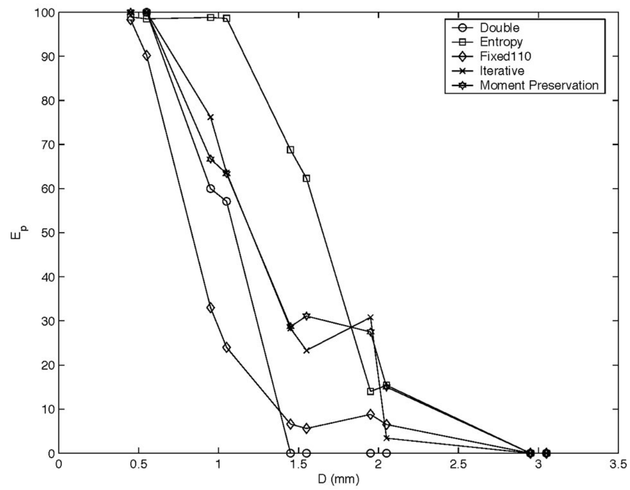

Fig. 20. Percentage error E_P in accepting out-of-focus drops as in focus for the bins of D shown.

and is plotted against D in Fig. 20. This figure shows that all algorithms have greater than 90% error in accepting drops with diameters below 1 mm. Hence, for these small diameters, the DSDs presented here should be considered in error. The error becomes zero for all the algorithms at $D = 3$ mm. For double thresholding, the percentage error becomes zero at $D = 1.4$ mm, and iterative and fixed thresholding both give less than 10% error at $D = 2$ mm. Entropy and MP thresholding algorithms gave the largest error in accepting out-of-focus drops. This large percentage also explains why these two algorithms have larger DSD values than double or fixed for smaller diameters (note the upward curvature of the DSD in Fig. 13 for these two methods). Double thresholding gives the lowest percentage error in accepting in-focus and consequently yields the lowest DSD values.

To prevent acceptance of out-of-focus drops we tested two smoothing algorithms to help to eliminate

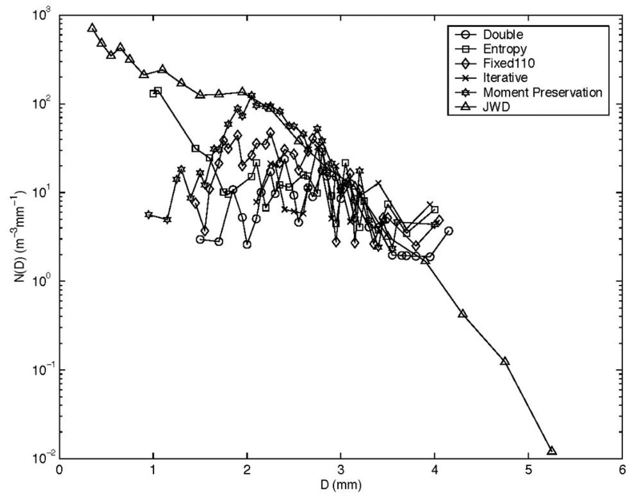

Fig. 21. DSDs for the rain that occurred during the 0th hour of 1 July after morphological closing was applied to smooth the images. The original DSDs are presented in Fig. 13.

Table 7. Rain Rates (mm h^{-1}) Obtained for Rain That Occurred During the 0th Hour of 1 July with the Simple Boundary Counting Algorithm and the Boundary Counting Algorithms with Image Smoothing[a]

Thresholding Algorithm	Boundary Counting	Boundary Counting with Closing	Boundary Counting with Yu–Yan Smoothing
Double	25.296	3.397	24.100
Entropy	53.176	3.640	51.982
Fixed 110	31.467	6.059	30.910
Iterative	44.987	2.940	43.448
MP	38.076	10.286	36.850

[a]The rain rate R calculated from the JWD for this hour was 19.594 mm h^{-1}.

spurious holes. Binary morphological closing smooths the object image by filling small gaps in the image. Figure 21 shows the DSDs for the rainfall during the 0th hour of 1 July after smoothing by morphological closing was performed on the images. The DSD values have decreased considerably and lie closer to the JWD curve. However, this new agreement is somewhat illusory because the smoothing process, while it increases the rejection of out-of-focus drops, also rejected many in-focus drops. This occurred because many in-focus drops have very small holes (<3–4 pixels), which close after this smoothing algorithm is applied. As a result, the DSD values are artificially decreased. The second smoothing algorithm tested was that of Yu and Yan.[34] This algorithm rejected images that had rough boundaries with notches [see, e.g., Fig. 19(c)]. However, it could not get rid of images that had false holes near the boundary that were one pixel in size [e.g., Figs. 19(a) and 19(b)]. The DSDs obtained with this smoothing algorithm for all the hours of rain data collected resulted in DSD plots that did not differ significantly from those presented in Fig. 21 and are not presented here. The rain rates that correspond to the DSDs presented in Fig. 21 are listed in Table 7. The elimination of holes near the edges of out-of-focus drops remains an unsolved problem.

Overall, the fixed and double thresholding algorithms examined here performed the best. On one hand, the fixed thresholding algorithm gave the least sensitivity of the dof to the drop diameter, and the slope of the linear relationship between the measured and actual drop diameters was closest to unity for this algorithm. On the other hand, the double thresholding algorithm gave the largest dof and the value of R obtained from this algorithm was closest to that obtained from the JWD than for any other algorithm. Additionally, the error from accepting out-of-focus drops was least for the double thresholding algorithm than from any of the other algorithms considered here.

5. Conclusions

Drop imagery obtained by use of a digital camera and a backlighting configuration was acquired in laboratory and field environments. We used the acquired data to evaluate the performance of five thresholding algorithms to determine their efficacy in the automated analysis of raindrop imagery. Laboratory data of MgF_2 spheres were used to quantify the depth of field and measurement accuracy of the system for each of the algorithms considered. Field data were acquired and used to show the accuracy in the measured rain rates and drop size distributions (DSDs).

The depth of field was found to be a function of the diameter in the diameter range 3–8 mm for all the algorithms investigated here, varying linearly with the diameter. The fixed thresholding algorithm gave the least sensitivity of the dof to the drop diameter. This method also gave the greatest similarity between the measured and actual drop diameters. The double thresholding algorithm gave the largest dof of all algorithms considered.

A comparative study of the thresholding algorithms showed significant differences between the DSDs from algorithm to algorithm and also between the algorithms and the JWD for diameters less than 3 mm. Part of this deviation may be due to the fact that the relationship between measured diameter and actual diameter was obtained in the laboratory for the diameter range 3–8 mm. Processing of field data, therefore, involved extrapolation of this relationship below the 3 mm diameter range. The double thresholding algorithm gave a value of rain rate that was closest to that obtained from the JWD than for any other algorithm. The relationship between the rain rate obtained from the algorithms and the rain rate obtained from the JWD was found to be linear for all thresholding algorithms explored here.

A significant obstacle to the use of these thresholding methods for the automated analysis of drop imagery is the large variation in the measured drop diameter over the depth of field. Reduction of this depth of field addresses this problem but reduces the number of raindrop measurements, which in turn makes it difficult to acquire a statistically converged DSD. Another problem left for future work concerns the acceptance of out-of-focus drops that have rough boundaries with deep notches or false holes. The smoothing algorithms applied to the images did not improve the results significantly, and a better approach is needed. Finally, note that the performance of the optical measurement system itself is not limited by the thresholding algorithms explored here. Significantly improved performance may be achieved with other algorithms, such as edge detection algorithms, and this remains a fruitful research direction.

Financial support for this work was provided by the National Science Foundation, Physical Meteorology program. The authors gratefully acknowledge the Joss–Waldvogel data provided by C. W. Ulbrich of Clemson University and the imaging equipment provided by L. F. Bliven of NASA. N. A. Sivasubramanian assisted in preparation of the figures for this manuscript.

References

1. R. J. Doviak and D. S. Zrnić, *Doppler Radar and Weather Observations* (Academic, 1984).
2. J. Joss and A. Waldvogel, "A raindrop spectrograph with automatic analysis," Pure Appl. Geophys. **68,** 240–246 (1967).
3. A. Tokay, A. Kruger, and W. F. Krajewski, "Comparison of drop size distribution measurements by impact and optical disdrometers," J. Appl. Meteorol. **40,** 2083–2097 (2001).
4. K. V. Beard and C. Chuang, "A new model for the equilibrium shape of raindrops," J. Atmos. Sci. **44,** 1509–1524 (1987).
5. C. Chuang and K. V. Beard, "A numerical model for the equilibrium shape of electrified raindrops," J. Atmos. Sci. **47,** 1374–1389 (1990).
6. M. Schönhuber, H. E. Urban, J. P. V. Poiares-Baptista, W. L. Randeu, and W. Riedler, "Measurements of precipitation characteristics by a new distrometer," in *Proceedings of Atmospheric Physics and Dynamics in the Analysis and Prognosis of Precipitation Fields* (SIMA, 1994).
7. J. R. Saylor, B. K. Jones, and L. F. Bliven, "A method for increasing depth of field during droplet imaging," Rev. Sci. Instrum. **73,** 2422–2427 (2002).
8. M. Schönhuber, H. E. Urban, J. P. V. Poiares-Baptista, W. L. Randeu, and W. Riedler, "Weather radar versus 2D-video-distrometer data," in *Proceedings of the Third International Symposium on Hydrological Applications of Weather Radars* (Wiley, 1995).
9. L. F. Bliven, (NASA, Wallops Island, Va. 23337 (personal communication, 2001).
10. J. R. Saylor, B. K. Jones, and L. F. Bliven, "Single-camera method to determine the optical axis position of ellipsoidal drops," Appl. Opt. **42,** 972–978 (2003).
11. R. Jain, R. Kasturi, and B. G. Schunck, *Machine Vision* (McGraw-Hill, 1995).
12. C. K. Leung and F. K. Lam, "Performance analysis for a class of iterative image thresholding algorithms," Pattern Recogn. **29,** 1523–1530 (1996).
13. N. J. Kapur, P. K. Sahoo, and A. K. Wong, "A new method for gray-level picture thresholding using the entropy of the histogram," Computer Vis. Graph. Image Process. **29,** 273–285 (1985).
14. P. Yin, "Maximum entropy-based optimal threshold selection using deterministic reinforcement learning with controlled randomization," Signal Process. 993–1006 (2002).
15. N. Ostu, "A threshold selection method from gray-level histograms," IEEE Trans. Syst. Man. Cybern. **9,** 62–66 (1979).
16. W. Tsai, "Moment-preserving thresholding: a new approach," Computer Vis. Graph. Image Process. **29,** 377–393 (1985).
17. P. Liao, T. Chen, and P. Chung, "A fast algorithm for multilevel thresholding," J. Information Sci. and Eng. **17,** 713–727 (2001).
18. L. K. Huang and M. J. J. Wang, "Image thresholding by minimizing the measure of fuzziness," Pattern Recognition **28,** 41–51 (1995).
19. O. J. Tobias and R. Seara, "Image segmentation by histogram thresholding using fuzzy sets," IEEE Trans. Image Process. **11,** 1457–1465 (2002).
20. C. Ho and L. Chen, "A fast ellipse/circle detector using geometric symmetry," Pattern Recogn. **28,** 117–124 (1995).
21. Y. Lei and K. C. Wong, "Ellipse detection based on symmetry," Pattern Recogn. Lett. **20,** 41–47 (1999).
22. E. R. Davies, *Machine Vision: Theory, Algorithms, Practicalities* (Academic, 1990).
23. H. K. Yuen, J. Illingworth, and J. Kittler, "Detecting partially occluded ellipses using the Hough transform," Image Vision Comput. **7,** 31–37 (1989).
24. K. V. Beard, H. T. Ochs, and R. J. Kubesh, "Natural oscillations of small raindrops," Nature **342,** 408–410 (1989).
25. K. V. Beard and R. J. Kubesh, "Laboratory measurements

of small raindrop distortion. 2. Oscillation frequencies and modes," J. Atmos. Sci. **48,** 2245–2264 (1991).
26. K. Andsager, K. V. Beard, and N. F. Laird, "Laboratory measurements of axis ratios for large raindrops," J. Atmos. Sci. **56,** 2673–2683 (1999).
27. J. Serra, *Image Analysis and Mathematical Morphology* (Academic, 1982).
28. F. Xia, "Normal vector and winding number in 2D digital images with their application for hole detection," Pattern Recogn. **36,** 1383–1395 (2003).
29. R. C. Weast, ed. *Handbook of Chemistry and Physics,* 52nd ed. (Chemical Rubber Company, 1971), Sec. B.
30. L. Samek and J. Wasylak, "Low-dispersion fluorozirconate glass with spectral dispersion of refractive index similar to that of water," Opt. Eng. **36,** 1657–1659 (1997).
31. J. Lucas, F. Smektala, and J. L. Adam, "Fluorine in optics," J. Fluorine Chem. **114,** 113–118 (2002).
32. J.-P. Thiran, V. Warscotte, and B. Macq, "A queue-based region growing algorithm for accurate segmentation of multidimensional digital images," Signal Process. **60,** pp. 1–10 (1997).
33. R. M. Haralick, S. R. Sternberg, and X. Zhuang, "Image analysis using mathematical morphology," IEEE Trans. Pattern Anal. Mach. Intell. **9,** 532–550 (1987).
34. D. Yu and H. Yan, "An efficient algorithm for smoothing, linearization and detection of structural feature points of binary image contours," Pattern Recogn. **30,** 57–69 (1997).
35. D. Atlas, R. C. Srivastava, and R. S. Sekhon, "Doppler radar characteristics of precipitation at vertical incidence," Rev. Geophys. Space Phys. **2,** 1–35 (1973).
36. C. W. Ulbrich, "Natural variations in the analytical form of the raindrop size distribution," J. Climate Appl. Meteorol. **22,** 1764–1775 (1983).